

Article

Effect of Oxygen Vacancy on the Crystallinity and Optical Band Gap in Tin Oxide Thin Film

Rajesh Dangi ^{1,†} , Bijaya Basnet ^{2,†} , Manoj Pandey ^{3,4}, Sandip Bhusal ¹, Biplab Budhathoki ¹ ,
Kshama Parajuli ^{1,*}, Santosh K. Tiwari ^{5,*}  and Bhim P. Kafle ^{4,*}

¹ Central Department of Chemistry, Tribhuvan University, Kirtipur 44618, Kathmandu, Nepal

² Advanced Materials and Liquid Crystal Institute, Kent State University, Kent, OH 44242, USA

³ Department of Physics, School of Science, Kathmandu University, Dhulikhel 45210, Kavre, Nepal

⁴ Department of Chemical Science & Engineering, School of Engineering, Kathmandu University, Dhulikhel 45210, Kavre, Nepal

⁵ Department of Chemistry, NMAM Institute of Technology, Nitte (Deemed to be University), Nitte 547110, Karnataka, India

* Correspondence: kshamaparajuli@yahoo.com (K.P.); ismgraphene@gmail.com (S.K.T.); bhim@ku.edu.np (B.P.K.)

† These authors contributed equally to the work.

Abstract: Herein, we have prepared tin oxide (SnO₂) nanoparticles (NPs), through a co-precipitation method, using SnCl₂·2H₂O dissolved in distilled water (DW) as a precursor. Then, the prepared NPs were heat treated in a muffle furnace, as a function of temperature, under an open atmosphere. The prepared SnO₂ NPs were then re-dispersed in DW, followed by spray casting on a glass substrate, for preparing SnO₂ thin films. The average thickness of the fabricated SnO₂ thin films was 2.76 μm. We demonstrated a very clear variation in the structural, compositional, and morphological features of the different films (in particular, variation of the density of oxygen vacancies), which altered their electrical and optical properties. Raising the calcination temperature of the SnO₂ thin films, from 250 °C to 650 °C, led to a monotonic reduction in the crystallite size, from 10.4 nm to 6.7 nm, and a decrease in the O/Sn ratio, from 5.60 to 4.79. A 14.5% decrease in the O/Sn ratio resulted in a decrease in the crystallite size by 3.7 nm (i.e., a 35.3% decrease in the NP size), and a decrease in the band gap of 0.11 eV. The lowering of the band gap, along with an increase in the oxygen vacancies in the films, accords well with previous studies. Besides, as the calcination temperature was raised, the refractive index and absorption coefficient values were also found to notably increase. Very interestingly, by simply altering the calcination temperature, we were able to produce SnO₂ thin films with optical band gaps nearly equal to the fundamental band gap (2.96 eV), even though many earlier experimental studies had reported considerably greater values (3.36–4.24 eV). SnO₂ thin films with lower oxygen vacancies exhibited relatively higher band gaps, which is likely to be favorable for the desired electron transport layer in perovskite solar cells.

Keywords: nanoparticles; thin film; calcination; oxygen vacancies; optical properties; crystallite size



Citation: Dangi, R.; Basnet, B.; Pandey, M.; Bhusal, S.; Budhathoki, B.; Parajuli, K.; Tiwari, S.K.; Kafle, B.P. Effect of Oxygen Vacancy on the Crystallinity and Optical Band Gap in Tin Oxide Thin Film. *Energies* **2023**, *16*, 2653. <https://doi.org/10.3390/en16062653>

Academic Editor: Senthilarasu Sundaram

Received: 16 November 2022

Revised: 11 February 2023

Accepted: 8 March 2023

Published: 11 March 2023



Copyright: © 2023 by the authors. Licensee MDPI, Basel, Switzerland. This article is an open access article distributed under the terms and conditions of the Creative Commons Attribution (CC BY) license (<https://creativecommons.org/licenses/by/4.0/>).

1. Introduction

The functional characteristics of metal oxides can be altered to a certain extent, by controlling the defect density and modifying the defect structure [1–3]. Because of their distinctive chemical, physical, and electrical properties; oxygen vacancies play a key role in establishing the physical characteristics of metal oxides, and serve as essential building blocks in several scientific and technological sectors [1]. It has been demonstrated over the past few decades, that many features of solid materials are governed by functional defects and imperfections in their crystal structure, in addition to their geometry and electronic structure [4–11]. Thus, the rapid advancement of semiconductor nanotechnology is likely to depend on our ability to manipulate materials' features, according to the nature and

density of defects [4,5]. Being one of the most prevalent defects in metal oxides, oxygen vacancies are the focus of both theoretical and experimental exploration [7–9]. Despite oxygen vacancies sometimes being assumed to be deleterious to the properties of oxides, such as in some magnetic oxides and dielectrics, it has been reported that they can also induce innovative features [1].

Along these lines, Choudhury et al. [12] reported that oxygen vacancies in CeO₂ nanoparticles (NPs) encouraged the lattice to expand (modification of the structural regularity), resulting in the red shift of the band gap and alteration of the material's visible luminescence. By using NaBH₄ treatment, Zeng et al. [13] were able to increase the oxygen vacancies without altering the oxides' crystal structure, morphology, or the specific surface area of NPs, for instance the specific surface area of pristine NPs was 6.19 m²g⁻¹ in Zeng et al.'s work, which improved the SnO₂ nanoparticles' ability to detect ethanol gas [13]. There, NaBH₄ treatment increased the surface oxygen vacancies, which facilitated oxygen adsorption and chemical reactions on the surface. Wei et al. [14], also noted that SnO₂ produced under vacuum had more oxygen vacancies than SnO₂ produced in air, and the sensor's NO₂ detection capabilities were greatly improved over those of the air-produced SnO₂ sensor.

Recently it has been reported that in-plane oxygen vacancies induce an anomalously high dielectric constant in SnO₂ nanoparticles, as found by Sahu et al. [15]. Schipani et al. [16] formed SnO₂ polycrystalline thin films with different work functions, by heat treatment in oxidizing or reducing environments (here, treatment altered the oxygen vacancies in the thin films). The temperature dependence of photoluminescence is significantly influenced by two different types of oxygen vacancies (at in-plane and out-of-plane sites, respectively) in nanowires [17]. The oxygen-vacancy-mediated fluorescence characteristics of SnO₂ nanowires, were found to depend on the temperature of heat treatment [17]. Similarly, Kumaravel et al. [18] showed that the addition of a foreign element to oxide NPs (for instance, doping Ir metal to TiO₂), lowers the formation energy of oxygen vacancies. Similarly, Vladislav et al. [19] found that oxygen vacancies can affect the electrical characteristics of semiconductor nanoparticles. According to Mahmood et al. [20], a higher number of oxygen vacancies, lowered the crystallite size and stabilized the tetragonal ZrO₂ phase. By injecting oxygen vacancies, Zhang et al. [21] achieved metallic properties in a WO₃ wide-gap semiconductor.

According to Zhu et al. [22], Ce doping increased the amount of oxygen vacancies, which led to increased catalytic activity in SnO₂ nanofibers. According to Elouafi et al. [23], Ru doping causes the oxygen vacancies to increase, which in turn causes the crystallite size and band gap in Fe₂O₃ powders to increase. On the other hand, in theoretical calculations, using a first-principle calculation using DFT, on ZnO nanocrystallites, Liu et al. [24] revealed that the formation energy of oxygen vacancies increased with increasing crystallite size.

Oxides were traditionally subjected to annealing in hydrogen, or other reducing environments, to alter the oxygen vacancy concentration in a given sample [25]. However, because of cost and safety concerns, the high temperature hydrogen annealing process is not preferable for practical applications. Some efficient alternative methods for creating additional oxygen vacancies on metal oxides have been developed, to solve the aforementioned issue [13]. For example, plasma treatment [26], annealing in vacuum [14], doping metals [27], and solution reduction techniques [28,29]. In addition to this, Liu et al. [30] modified the oxygen vacancies of SnO₂ using a novel approach powered by organometallic chemistry, for electrochemical applications. Additionally, by adjusting the rate at which liquid SnCl₄ hydrolyzed, Li et al. created oxygen vacancies-enriched SnO₂ nanoparticles, for NO₂ gas sensing applications [31].

In prior publications [32–36], SnO₂ has been referred to as an n-type wide-band gap semiconductor, with an optical band gap of 3.60–4.24 eV. The band gap values obtained in these studies are significantly higher than the fundamental band gap calculated by Cai et al. [32], using first-principles calculations, in the most recent studies (3.0 eV). In the current work, for the first time, we report SnO₂ thin films with optical band gaps that

are close to the fundamental band gap. We found that, the unexpectedly higher optical band gaps of SnO₂ thin films reported in the previous literature, were caused by a different amount of oxygen vacancies formed during, either the deposition process, the calcination environment, the post-processing environment, or a combination of them. To note, the SnO₂ thin film, with lower oxygen vacancies and a relatively higher optical band gap, reported in this work, is suitable for the ETL layer in perovskite solar cells.

In the present work, we demonstrate the relationship between crystallite size and oxygen vacancies in SnO₂ nanoparticles, as a function of calcination temperature. It is noteworthy to mention that calcination results in the formation of oxygen vacancies in the crystals of SnO₂ NPs. These vacancies can exist as neutral (V_o), singly (V_o^-), or doubly charged (V_o^{2-}), and give rise to several donor levels within the forbidden energy gap [37]. Here, singly and doubly charged vacancies act as deep donors, while neutral vacancies act as shallow donors [37,38]. We also explored the tuning of the band gap by varying the oxygen defect density. We have synthesized the SnO₂ nanoparticles via a chemical precipitation method [39], and fabricated thin film on a glass substrate by using spray pyrolysis. Then we have studied their structural, morphological, and optoelectronic properties, keeping in mind the application in perovskite solar cells, as an electron transport layer (ETL).

2. Experimental Detail

2.1. Material Preparation

Chemicals: Tin dioxide dihydrate (SnCl₂·2H₂O), from Alfa Aser, ammonia solution (25%), acetone (97%), triple deionized (DI) water, and ethanol (99%), from Merck (India), and isopropanol, from Fisher Scientific, were used.

Glass substrate: The commercially available ordinary microscopic glass slides were cut into pieces, with dimensions of 2 cm × 2 cm × 1 mm, and properly cleaned with detergent water. They were washed with alcohol, isopropanol, and ultrasonicated for 15 min with acetone, followed by rinsing with deionized water, to clean the dirt on the glass substrates. The cleaned substrates were stored by soaking in distilled water, and were air dried before use.

Spray pyrolysis: A home-made spray pyrolysis setup was housed inside a wooden chamber, with dimensions of 75 cm × 40 cm × 30 cm. The spray system was combined with an electrically heated movable thick rectangular iron plate, on which a glass slide was placed for coating. A temperature sensor was attached to the middle of the iron plate. For controlling the temperature of the substrate, a temperature controller was used. The pressure needed to generate aerosol was maintained with the help of a nebulizer, with the desired pumping capacity, which can spray SnO₂ colloidal solution. The colloidal solution was housed in a plastic vessel, with a capacity of 10 mL, which was connected directly to the nebulizer. The nebulizer was then connected to a glass nozzle through a plastic pipe, whose nozzle diameter was ~1 mm. The substrate to nozzle distance was maintained at 5 cm above the substrate, which lay just above the metal plate [40].

2.2. Preparation of SnO₂ NPs and Thin Films

SnO₂ powder NPs were prepared by the chemical precipitation method, as reported elsewhere [39]. In brief, white solid crystals of SnCl₂·2H₂O (4 g) were dissolved in deionized (DI) water, to make a 0.1 M solution. Then 100 mL of DI water was added slowly, along with magnetic stirring, followed by ultrasonication for about 10 min, to make the solution homogeneous. Here, the pH of the solution was observed to be 1.6. Then 25% NH₃ solution was added drop-wise, along with continuous stirring and heating at 25 °C for 40 min. A white gelatinous precipitate was observed, and at this stage the pH of the suspension was 9.2. The precipitate was left overnight to settle down. Then the precipitate was washed by a centrifugation process (three times at 4500 rpm for 5 min each), followed by filtration and washing the precipitate with deionized water 3 times. The precipitate was left to dry in a furnace at 80 °C for 12 h. The dry SnO₂ was ground by pestle and divided into three equal

parts. Then the three samples were calcined at low (250 °C), medium (450 °C), and high (650 °C) temperatures, respectively.

For preparing thin film from the above three kinds of SnO₂ samples, 30 mg of powder of each sample was dissolved in 30 mL deionized water, separately. The suspension was stirred for 30 min by a magnetic stirrer, followed by ultrasonication for 5 min, to make a uniformly dispersed solution. These three new SnO₂ suspensions were transferred into separate glass vials, for making them ready for spray pyrolysis. Then, the SnO₂ colloidal solutions were sprayed on a hot glass substrate, at a temperature of 400 ± 5 °C, for up to 15 s, followed by a rest for 30 s, to maintain the substrate temperature by spray pyrolysis.

2.3. Characterization

For studying the crystallinity of the SnO₂ nanoparticles deposited on the glass substrates, an XRD, from Bruker D2 phase diffractometer, Berlin, Germany, was employed. The surface morphology and chemical compositions were analyzed, respectively, by scanning electron microscopy (SEM) and energy dispersive spectroscopy (EDS), from (JSM-IT 100), JEOL, Tokyo, Japan. Fourier-transform infrared spectroscopy (FTIR), from IRprestige-21, (SHIMADZU), Kyoto, Japan, was used for identifying functional groups in the final product. The optical transmittance and reflectance of the thin film were obtained by an optical profilometer (Abet Technology, Milford, CT, USA).

3. Results and Discussion

3.1. Structural Properties

a. X-ray diffraction pattern

The crystallographic features of powder SnO₂ NPs were characterized by scanning between 2θ (20–80°), by an X-ray diffractometer (Bruker D2 phase, Germany), using CuKα radiation of wavelength 1.5406 Å, at room temperature. The XRD spectra of the NP samples calcined at three different temperatures (250 °C, 450 °C, and 650 °C) are shown in Figure 1. The peak positions show good agreement with JCPDS card no. 41-1445 of SnO₂ [39]. The diffraction peaks at 2θ = 26.6°, 33.9°, 37.9°, 51.8°, 54.5° and 61.9° are associated with (110), (101), (200), (211), (220), (310), respectively, indicating a tetragonal structure of SnO₂ NPs [41,42]. As depicted in Figure 1, the intensity of all the diffraction peaks increased with increasing calcination temperature. The average crystallite size was calculated from all diffraction peaks, using Scherrer's formula [43,44].

$$D = \frac{K\lambda}{\beta \cos\theta} \quad (1)$$

where D is the crystallite size, K is the shape factor (the Scherrer constant), equal to 0.9, λ is the X-ray wavelength for the CuKα radiation applied (0.15406 nm), β is the full width at half maximum (FWHM) of the observed peak (in radians), and θ is the Bragg's diffraction angle (peak position) in degrees. To note, the value of β was estimated by employing Gaussian fitting for all the peaks, as previously reported [45]. Then its observed value was placed in Equation (1), to estimate the D of the NPs at that particular plane of Bragg's reflection, as crystallite size also depends on lattice planes/orientation [46].

It is noteworthy to mention, that the Scherrer constant, or shape constant K , varies between 0.6 and 2.0 depending on the shape of the crystallite and the type of the crystal [47–50]. For example, the crystallite can take the shape of a sphere, cube, tetrahedron, octahedron, rectangular parallelepiped, cylinder, triangular prism, square prism, and hexagonal prism [47,48]. Muniz et al. [51] discussed the limit on the applicability of the Scherrer equation. Londoño-Restrepo et al. [52] demonstrated the Scherrer equation to be one of the reliable methods of determining the crystallite size. The Scherrer constant is taken as 0.9, as derived in Scherrer's original paper [53–55]. Most of the literature has used $K = 0.9$ to calculate the average crystallite size, with the geometry similar to ours [54–61]. The Scherrer method determines the average crystallite size with a higher accuracy, of ±15%, when the shape constant, K , is taken as 0.9 for a rutile structure [61].

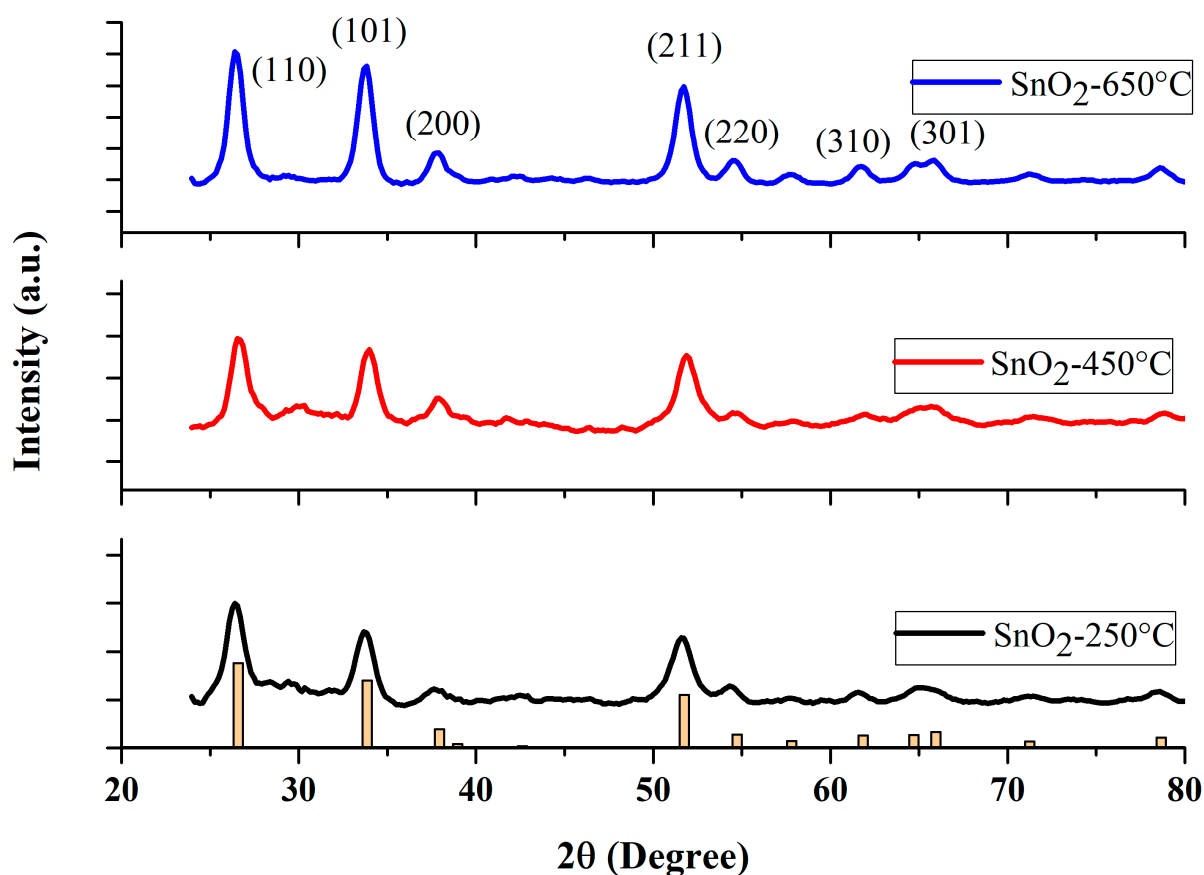


Figure 1. XRD patterns of the SnO₂ nanoparticles at various calcination temperatures. (Yellow bar chart represents the diffractogram of the JCPDS card).

The average value of D was estimated by averaging all the D values of the peaks appearing in the sample at a given condition. No impurity peaks were observed, indicating the fair purity of the final products. The values of crystallite sizes of the SnO₂ samples sintered at three different temperatures are summarized in Table 1. From a close look at the XRD data, one may infer that there is no secondary phase present in our samples. The nanoparticles prepared at the lowest temperature (250 °C) of our study, showed rather broad peaks, when compared with the other two samples. This situation altered noticeably when the temperature was increased to 450 °C and 650 °C. The enhancement in the peak intensity with diminished peak widths, indicates that our NPs calcined at high temperatures, yielded NPs with high crystallinity, in agreement with standard values [62].

Table 1. Crystallite size of SnO₂ nanoparticles calcined at 250 °C, 450 °C, and 650 °C.

Samples	Average Crystallite Size (D , nm)
SnO ₂ (250 °C)	6.71 nm (± 0.13 nm)
SnO ₂ (450 °C)	8.34 nm (± 0.17 nm)
SnO ₂ (650 °C)	10.37 nm (± 0.35 nm)

The average crystallite sizes of SnO₂ NPs calcined at 250 °C, 450 °C, and 650 °C were found to be 6.71 nm, 8.34 nm, and 10.37 nm, respectively, shown in Table 1. The comparatively smaller values of the NPs' size can be mainly attributed to factors such as temperature, pressure, pH, solvent, and time [62–65].

Sahu et al. [15] observed that, when SnO₂ NPs samples were annealed in argon and air, the crystallite size increased, and the band gap decreased, as observed in the present study. Therefore, we may safely state that larger crystallite sizes result in a smaller band gap.

Doping a foreign element, such as Cr in ZnO, can reduce the crystallite size, by altering the rate of nucleation during the crystallization of the sample, decelerating the formation of grain boundaries, or by modifying the geometrical structure of the crystal lattice, as lattice strain is anticipated to change with the addition of the foreign element [66]. As calcination does not involve the doping of any foreign element in the host matrix, solely thermal treatment is responsible for the shift in Sn:O composition and crystallite size seen here.

b. FTIR

Functional group identification of the sample materials was performed by FTIR spectroscopy, in the wavelength range $4000\text{--}400\text{ cm}^{-1}$. The SnO_2 powder samples calcined at temperatures of $250\text{ }^\circ\text{C}$, $450\text{ }^\circ\text{C}$, and $650\text{ }^\circ\text{C}$, were taken for FTIR analysis. Figure 2 shows the FTIR spectra of the SnO_2 NPs calcined at different temperatures. The broad band around 3400 cm^{-1} was correlated with the stretching vibration of the --OH groups of Sn(OH)_2 , and adsorbed water molecules on the surface of the SnO_2 sample powder of low calcined temperature (particularly at $250\text{ }^\circ\text{C}$). The decrease in the peak intensity suggests the removal of --OH groups from the sample through evaporation, at high temperature. The lowest band, between 456 cm^{-1} to 464 cm^{-1} , has been attributed to the O–Sn–O or Sn–O stretching vibration band of SnO_2 [67]. The bands at 464 cm^{-1} , 460 cm^{-1} , and 456 cm^{-1} are shown in Figure 2, to show the absorption of the FTIR spectrum caused by the Sn–O stretching. The slight shift in the absorption valley could be attributed to the change in the O/Sn ratio caused by the calcination. Moreover, at the higher temperature of our study range, the later peaks became broader, indicating the formation of pure and crystalline SnO_2 powder at high temperature [68]. The absence of any other sharp peaks in all the three FTIR spectra, indicates the absence of any other functional groups in the samples [69].

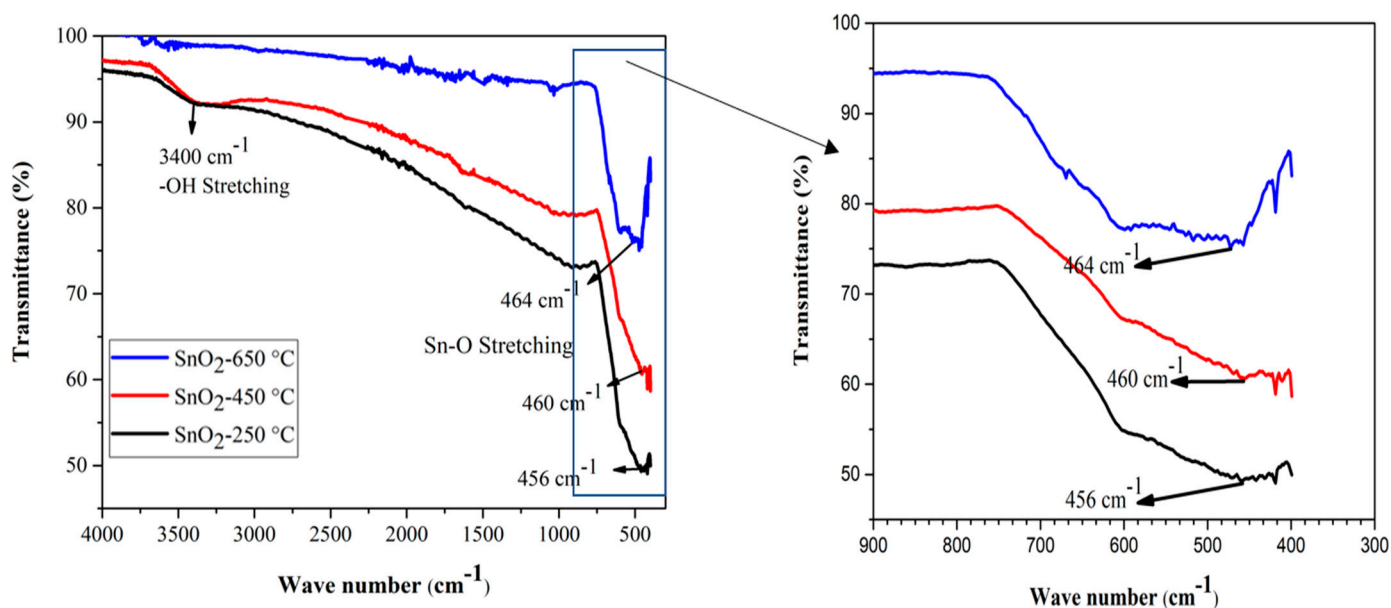


Figure 2. FTIR spectra of SnO_2 nanoparticles at various calcination temperatures.

3.2. Morphological Properties

The surface morphology of the SnO_2 nanomaterials calcined at $250\text{ }^\circ\text{C}$, $450\text{ }^\circ\text{C}$, and $650\text{ }^\circ\text{C}$, was studied by SEM analysis (Figure 3). The SEM images of the samples reveal the formation of spherical shapes of SnO_2 particles, which agglomerated to form clusters (Figure 3). The formation of the clusters was due to the nucleation of the NPs and growth of the nucleated particles [64]. The qualitative chemical composition of the SnO_2 samples determined by FTIR, presented in Figure 2, was further confirmed by EDX measurements. The composition of SnO_2 NPs estimated from EDS analysis are shown in Table 2. The spectra from these measurements, for all the three samples, were found to possess the signals from Sn and O only. No additional peaks corresponding to any other elements

were observed, indicating no other impurity being present in any of the three samples. Remarkably, we found that increasing the calcination temperature from 250 °C to 650 °C, resulted in a decrease in the oxygen content of 2.5% (i.e., the O/Sn ratio decreased from 5.60 to 4.79; in other words, it increased the oxygen vacancies). The change in O/Sn ratio as a function of the calcination temperature, is responsible for changing the band gap, which is discussed later.

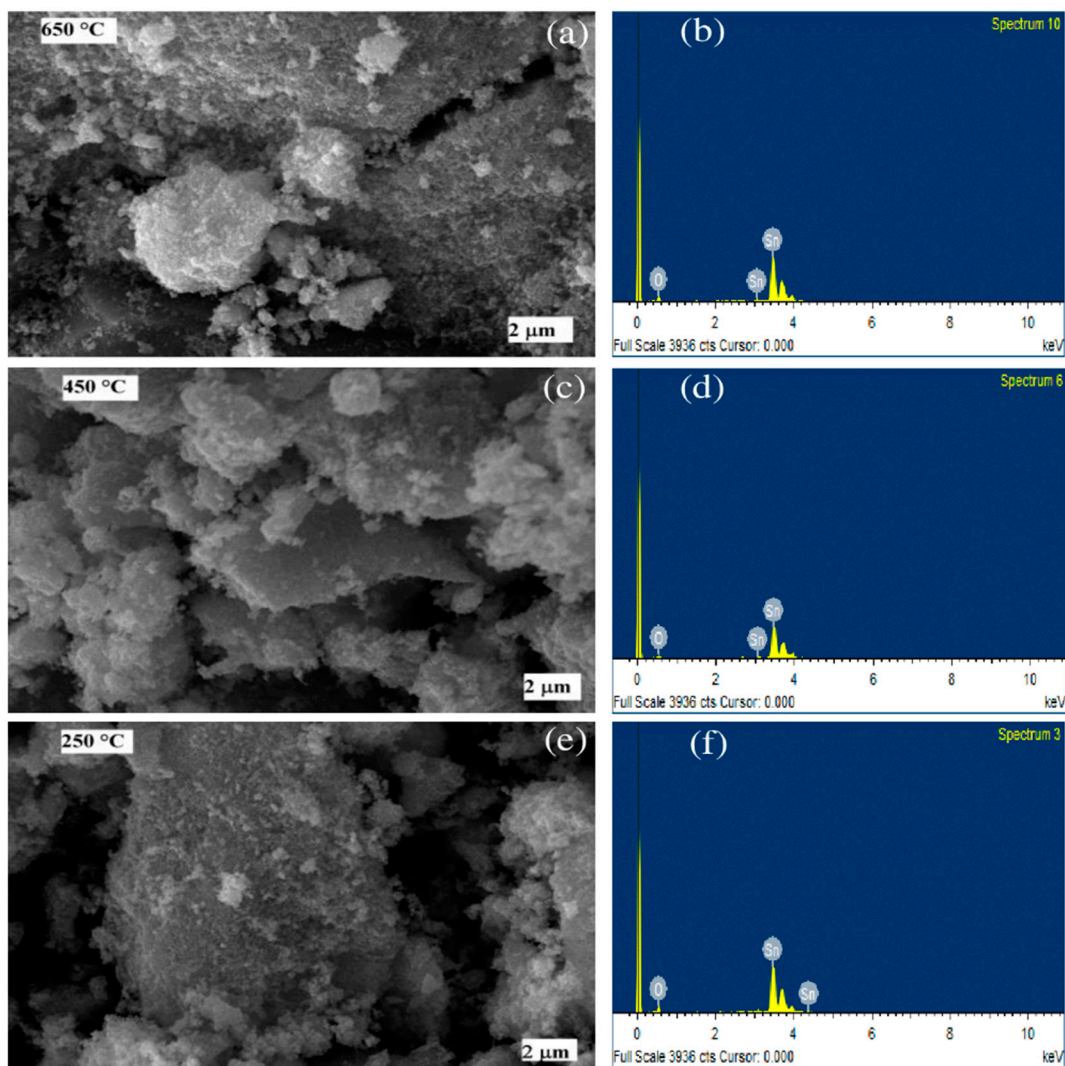


Figure 3. SEM images (left, (a,c,e)) and EDS spectra (right, (b,d,f)) of the SnO₂ nanoparticles formed at calcination temperatures of 650 °C, 450 °C, and 250 °C.

Table 2. The composition of SnO₂ NPs estimated from EDS analysis. Here, errors represent elements other than Sn and O.

Samples	Sn (At. %)	O (At. %)
SnO ₂ (250 °C)	15.15 (±0.00)	84.85 (±0.00)
SnO ₂ (450 °C)	15.36 (±0.00)	84.64 (±0.00)
SnO ₂ (650 °C)	17.26 (±0.00)	82.74 (±0.00)

In agreement with our results, Khan et al. [70] reported that, with increasing the calcination temperature from 400 °C to 800 °C, SnO₂ nanoparticles' crystallite size increased from 11.96 nm to 35.90 nm. Similarly, also in the case of CeO₂ nanoparticles, Choudhury et al. [71] reported a rise in crystallite size with increased annealing temperature, as well

as decreasing oxygen vacancies, lattice constant, and lattice strain. Note that the lattice parameter and the strain are directly proportional to each other [72]. As the oxygen vacancies in SnO₂ nanoparticles increase, the crystallite size also increases.

The dynamics of ionic defects, the exchange of oxygen from or into the environment, and the transfer of electronic charges from or into the material, all play a role in the generation and annihilation of oxygen vacancies in transition metal oxides [1]. The involvement of these multiple processes make a complex solid-state redox process [7]. It has been understood that the two electrons that were once connected to the oxygen ion stay in the oxide, even after oxygen is removed [1,7]. These electrons, generated by removing oxygen, populate defect states that, in wide-band gap oxides, are frequently found inside the band gap (in-gap states) [1,73,74]. The electrons can delocalize into the oxide's conduction band when these donor states are shallower, increasing the material's electrical conductivity [1,7,75]. As a result, these n-type oxides can exhibit an insulator-to-metal transition at a few ppm (10¹⁶ to 10¹⁸ cm³) of oxygen vacancies, and are predicted to exhibit even greater conductivity at higher vacancy concentrations [10,76,77]. Due to the fact that SnO₂ is also an n-type semiconductor with a wide band gap [11], the higher concentration of oxygen vacancies obtained by increasing the calcination temperature, minimizes the band gap, as will be discussed in more detail in the next section. On the other hand, increased oxygen vacancy concentrations in p-type oxides, often result in a metal-to-insulator transition, because they lower the material's hole concentration [1].

3.3. Optical Properties

To investigate the effect of calcination temperature on the optical properties, we measured the reflectance and transmittance spectra of the SnO₂ thin films, which were calcined at 250 °C, 450 °C, and 650 °C, shown in Figure 4a,b. Apparently, one can notice the interference pattern in the reflectance spectra, between 550 nm and 1050 nm. In order to extract other optical properties, particularly, the refractive index, absorption coefficient, film thickness, and optical band gap of a particular sample, we employed the Minkov algorithm [78]. For this, we generated an envelope using the cubic spline method, shown in Figure 4a with dotted lines, as demanded by the algorithm.

For a very thin film, deposited on a transparent substrate of a finite dimension, and with a very weak absorption coefficient, the thickness, d , and complex refractive index, $n = n - ik$, the reflectance, R [78], and transmittance, T [79–82], for the normal incidence of the light, can be represented as,

$$R = \frac{A' - (B'_1 \cos(2\delta) - B'_2 \sin(2\delta))x + C'x^2}{A'' - (B''_1 \cos(2\delta) - B''_2 \sin(2\delta))x + C''x^2} + \frac{A'''x^2}{A'' - (B''_1 \cos(2\delta) - B''_2 \sin(2\delta))x + C''x^2} \times \frac{1}{D'' - (E''_1 \cos(2\delta) - E''_2 \sin(2\delta))x + F''x^2} \quad (2)$$

where

$$\begin{aligned} A' &= [(n-1)^2 + k^2] [(n+n_s)^2 + k^2] \\ B'_1 &= 2[(n^2 + k^2 - 1)(n^2 + k^2 - n_s^2) + 4k^2n_s] \\ B'_2 &= 4k[n_s(n^2 + k^2 - 1) - (n^2 + k^2 - n_s^2)] \\ C' &= [(n+1)^2 + k^2] [(n-n_s)^2 + k^2] \\ A'' &= [(n+1)^2 + k^2] [(n+n_s)^2 + k^2] \\ B''_1 &= 2[(n^2 + k^2 - 1)(n^2 + k^2 - n_s^2) - 4k^2n_s] \\ B''_2 &= 4k[n_s(n^2 + k^2 - 1) + (n^2 + k^2 - n_s^2)] \end{aligned}$$

$$\begin{aligned}
C'' &= [(n-1)^2 + k^2] [(n-n_s)^2 + k^2] \\
A''' &= 64n_s(n_s-1)^2 (n^2 + k^2)^2 \\
D'' &= [(n+1)^2 + k^2] [(n+1)(n+n_s^2) + k^2] \\
E_1'' &= 2[(n^2 + k^2 - 1)(n^2 + k^2 - n_s^2) - 2k^2(n_s^2 + 1)] \\
E_2'' &= 2k[(n^2 + k^2 - n_s^2) + (n_s^2 + 1)(n^2 + k^2 - 1)] \\
F'' &= [(n-1)^2 + k^2] [(n-1)(n-n_s^2) + k^2] \\
x &= e^{-\alpha d} \\
\delta &= 2\pi n d / \lambda \\
k &= \frac{\alpha \lambda}{4\pi} \\
T &= \frac{A'''' x}{A'''' - (B_1''' \cos(2\delta) - B_2''' \sin(2\delta))x + D''' x^2} \quad (3)
\end{aligned}$$

where

$$\begin{aligned}
A'''' &= 16n_s(n^2 + k^2) \\
A'''' &= D'' \\
B_1''' &= E_1'' \\
B_2''' &= 2k[2(n^2 + k^2 - n_s^2) + (n_s^2 + 1)(n^2 + k^2 - 1)] \\
D''' &= F'' .
\end{aligned}$$

Here, n and k are, respectively, the refractive index and extinction coefficient of thin film, n_s is the refractive index of the glass substrate, α is the absorption coefficient of the thin film, and λ is the wavelength of the light.

For the weak and medium absorption region of the reflection spectra (550–1050 nm) in Figure 4a, $k \ll n_s$ and $k \ll n$, the maximum, R_M , and minimum, R_m , of the reflectance [78] can be written as,

$$R_M = \frac{(ad + bcx)^2}{(bd + acx)^2} + \frac{gx^2}{(bd + acx)^2(b^3f + 2abcdx + a^3ex^2)} \quad (4)$$

$$R_m = \frac{(ad - bcx)^2}{(bd - acx)^2} + \frac{gx^2}{(bd - acx)^2(b^3f - 2abcdx + a^3ex^2)} \quad (5)$$

where $a = n - 1$, $b = n + 1$, $c = n - n_s$, $d = n + n_s$, $e = n - n_s^2$, $f = n + n_s^2$, and $g = 64n_s(n_s - 1)^2 n^4$. We have calculated the refractive index and the absorption coefficient values in the transparent region by solving the non-linear Equations (4) and (5), using the well-known Newton–Raphson iteration, with an initial guess of $n = 2.0$ and $x = 0.5$. Refractive indices and absorption coefficients were further corrected using the Minkov algorithm [78], whose accuracy is 0.2% for the refractive index and 1.5% for the absorption coefficient. Note that the refractive index of the glass substrate was taken to be 1.5.

In the weak and medium absorption region of the reflectance spectra, a reduction in the calcination temperature also resulted in a reduction in the average values of the maxima R_M (i.e., 10.2%, 9.0%, and 8.9% for 650 °C, 450 °C, and 250 °C, respectively) and minima R_m (i.e., 9.5%, 8.3%, and 8.2% for 650 °C, 450 °C and 250 °C, respectively). In the strong absorption region (i.e., 350–550 nm), we observed interference free reflectance. In addition,

we found that lowering the calcination temperature from 650 °C to 250 °C, resulted in a decrease in the reflectance, implying that a reduction in the calcination temperature lowers the thin film's refractive index [83]. The refractive indices extracted from the Minkov algorithm [78], shown in Figure 4c, also confirm that lowering the calcination temperature reduces the SnO₂ film's refractive index.

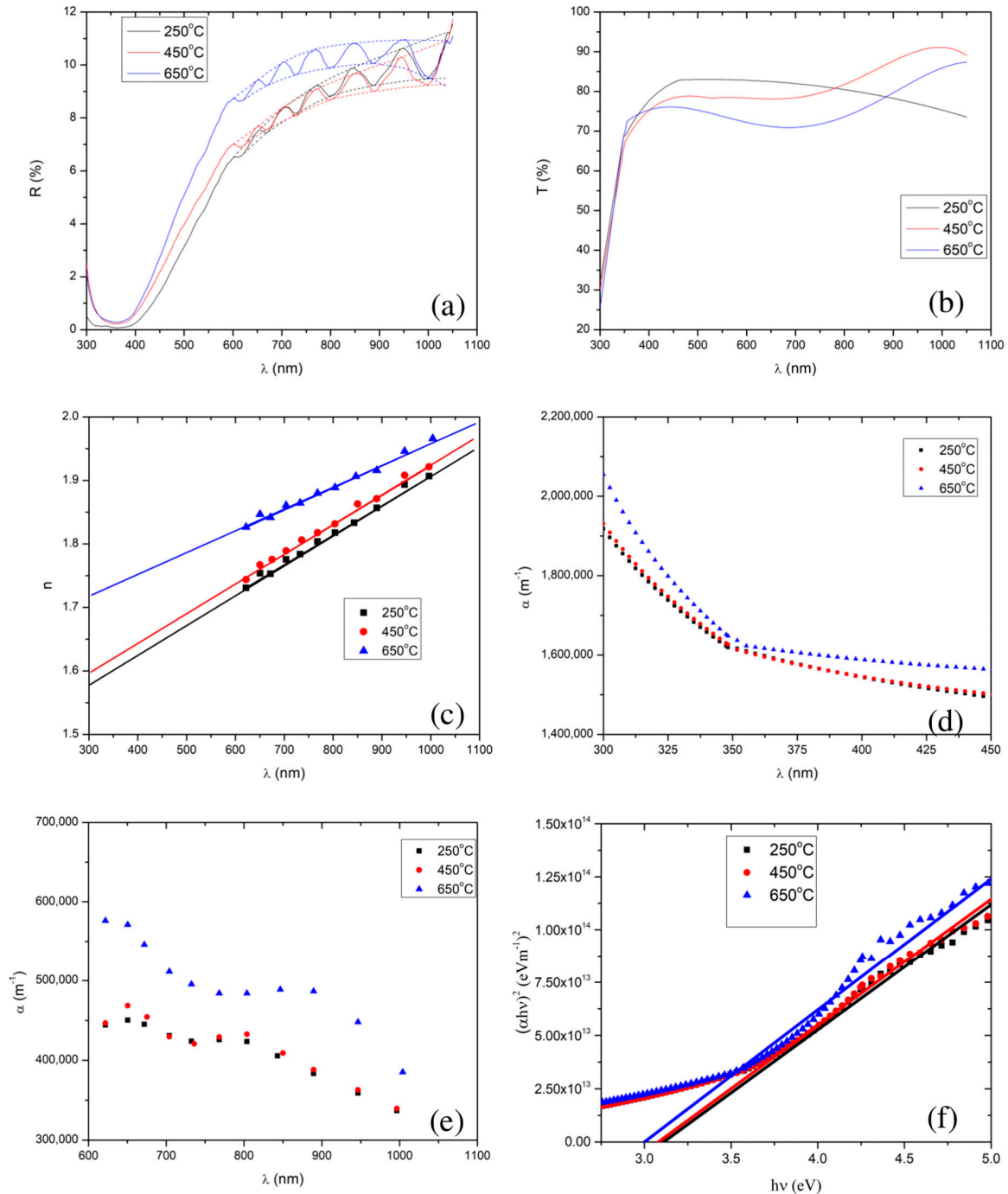


Figure 4. Plots (a) and (b) show the reflectance and transmittance spectra, respectively, of the SnO₂ thin films calcined at 250 °C, 450 °C, and 650 °C. Plots (c) and (d) show the refractive index and absorption coefficient, respectively, as a function of wavelength, which are extracted from the reflectance spectra. Plots (e) and (f) show the absorption coefficient and Tauc plot, respectively, which are extracted from the transmittance spectra. Note that in (a), the reflection spectra are denoted by solid lines, and the upper and lower limits of an envelope of each reflectance curve are denoted by the dotted lines.

We have calculated the thickness of the thin film [78] as follows,

$$d = \frac{\lambda_1 \lambda_2}{4(\lambda_1 n_2 - \lambda_2 n_1)} \quad (6)$$

where λ_1 and λ_2 are the wavelengths of the two adjacent extrema (i.e., neighboring maxima and minima), and n_1 and n_2 are their respective refractive indices of the thin film.

The extracted thicknesses of the films, for 250 °C, 450 °C, and 650 °C calcination temperatures, were 2.87 μm , 2.85 μm , and 2.55 μm , respectively. Increasing the calcination temperature slightly reduced the film's thickness ($0 < \Delta d < 0.32 \mu\text{m}$). The change in film thickness with calcination temperature was less than 12%. In addition, the absorption coefficients for different calcination temperatures, extracted from the reflectance in the weak and medium absorption regions, are shown in Figure 4d. The average values of the absorption coefficients are $4.98 \times 10^5 \text{ m}^{-1}$, $4.16 \times 10^5 \text{ m}^{-1}$, and $4.12 \times 10^5 \text{ m}^{-1}$, for 650 °C, 450 °C, and 250 °C, respectively.

Additionally, we have verified our calculation of the thicknesses and refractive indices by calculating the extremum order [78,84], as follows.

$$m = \frac{4nd}{\lambda_{extr}} \quad (7)$$

The extremum order for the minima and maxima of the reflectance spectra should be, respectively, even and odd integer numbers. The extremum orders of two neighboring maxima and minima should differ by 1. The extremum order should increase on moving from the IR region to the UV region.

In 1986, Kushev et al. [84] demonstrated that their theoretical model (based on envelope of reflectance measurement) could estimate film thickness with an accuracy of better than 1.0%. Similarly, Minkov [78] also established that the envelope method, based on reflectance, could compute the thickness with an accuracy of 0.2%. In both of these theoretical works, the authors considered thin films, which were deposited over a substrate of known optical parameters (such as refractive index and absorption coefficient) and film thicknesses. Then, employing these known optical parameters and thicknesses, the authors simulated each films' reflectance spectrum, and then applied their algorithm on the simulated reflectance curve to calculate the thickness and optical parameters of that particular thin film. Please note that Kushev et al. [84] and Minkov [78] both considered slightly absorbing thin films, coated over a transparent substrate, which is a good approximation for our study as well, as our thin films, of SnO_2 coated over a glass substrate, are semi-transparent. However, the thickness (and other optical parameters such as refractive index and absorption coefficient) extracted from both of these models possibly deviate; specifically in the cases in which the substrates possess some light absorption and the thin films have a greater absorption coefficient at the absorption edge.

In this connection, recently Borah et al. [85], performed the three different techniques, namely the Tolansky method [85,86], Swanepoel's envelope method [79], and the cross-sectional SEM method [85], to measure the thickness of molybdenum oxide thin films, deposited on a clean glass substrate. In their study, the thicknesses of the thin films ranged between 1.5 μm and 6 μm . For a particular sample, they employed the Tolansky method [85,86], Swanepoel's envelope method [79], and the cross-sectional SEM method [85], and observed 2.1 μm , 2.3 μm , and 2.4 μm thicknesses, respectively. Note that the Swanepoel's envelope method [79] reports 4% to 24.5% deviation from the cross-sectional SEM method: the 4% deviation was noticed for the sample with a higher number of interference patterns, whereas the 24.5% deviation was noticed for the sample with a lower number of interference patterns in a given transmittance spectrum [85]. These observations further imply that the envelope method could serve as a reliable method to calculate the film thickness.

Note that, Minkov's envelope method [78] also considers the same geometry and optical parameters in the system of thin film and substrate as used by the Swanepoel's

envelope method [79]. The only difference between Minkov's envelope method [78] and Swanepoel's envelope method [79], is that the former uses the reflectance spectrum while the later model uses the transmission spectrum. As a result, Minkov's envelope method [78] and Swanepoel's envelope method [79] are expected to have more or less the same accuracy for the thickness calculation.

It is noteworthy to mention that sprayed nanoparticles have different crystallite sizes depending on the calcination temperature. As a result, the small decrease in thin film thickness on increasing the calcination temperature of the nanoparticles, could be attributed to the effect of the calcination, which produced different ratios of Sn:O. Gnanam et al. [87], Kafle et al. [40], Xin et al. [88], and El-Nahass et al. [89] showed the dependence of the crystallite size on the film thickness and calcination temperature. In our work, although small, we observed a noticeable dependence of the film thickness on the crystallite size of the NPs, which is most likely as a result of the calcination temperature.

In the visible region (350–800 nm) of the solar spectrum, the average transmittance of the films was found to be 73.3%, 77.8%, and 81.1%, for the films calcined at 650 °C, 450 °C, and 250 °C, respectively, i.e., there was a decrease in average transmittance with an increase in calcination temperature. This decrease in average transmittance with increase in calcination temperature resulted from an increase in the refractive index and absorption coefficient (see in Figure 4c,d).

In the strong absorption region of the transmission spectrum (300–450 nm in Figure 4b), the transmittance [79] is written as,

$$x \approx \frac{(n-1)^3(n+n_s^2)}{16n^2n_s}T \quad (8)$$

The absorption coefficient in the strong absorption region is written as,

$$\alpha = \frac{-\ln(x)}{d} \approx \frac{-1}{d} \ln \left(\frac{(n-1)^3(n+n_s^2)}{16n^2n_s}T \right) \quad (9)$$

The absorption coefficient in the strong absorption region is extracted using Equation (8), shown in Figure 4e. Note that, we have extrapolated the plot of n vs. λ for the refractive index's values in the strong absorption regions, shown in Figure 4c. We observed that increasing the calcination temperature led to an increase in the absorption coefficient in the strong absorption region, although the values of the absorption coefficient for the 250 °C and 450 °C calcined films are very close. The band gaps of the thin film samples were extracted by extrapolation fitting the linear model to the curve of $[\alpha hv]^2$ vs. photon energy (hv) (the well known Tauc plot [90–92], defined by Equation (10)) shown in Figure 4f.

$$\alpha hv = A(hv - E_g)^{1/2} \quad (10)$$

Here, A , h , and v are, respectively, a constant, Planck's constant, and the frequency of the radiation.

We have employed the least-squares fitting between 3.6 eV and 5.0 eV to draw the tangent at the strong absorption region in the Tauc plot. One can use the R squared value to find the goodness of the fit in the least-squares fitting, and also can find the maximum error for the determination of the band gap. R squared was found to be 0.98, 0.99, and 0.98 for the thin films of SnO₂ NPs calcined at 250 °C, 450 °C, and 650 °C, respectively. Here, it is noteworthy to mention that, an R squared of 1 represents the perfect fit. The band gap values were respectively found to be 3.11 (± 0.07) eV, 3.08 (± 0.04) eV, and 3.00 (± 0.07) eV.

We found that the SnO₂ thin films exhibited direct band gaps, and the extracted values of the band gaps are shown in Figure 4f, for all the calcination temperatures. We observed band gaps of 3.00 eV, 3.08 eV, and 3.11 eV, for the calcination temperatures of 650 °C, 450 °C, and 250 °C, respectively. This further confirms the lowering of the band gap with an increase in the calcination temperature. Al-Hada et al. [68] also reported

similar results: a decrease in the band gap of SnO₂ nanoparticles with an increase in the calcination temperature, although, their band gap values were rather high (3.90 eV to 3.64 eV) compared to those in the present study.

Cai et al. [32] made a genuine effort to solve the long-standing band gap problem of SnO₂, using first-principles calculations with different levels of computational methods. The authors found that the fundamental band gaps of SnO₂ and TiO₂ are nearly the same (i.e., around 3.0 eV), as both of them have the same rutile structure (see their band structures in Figure 5). Whereas, other researchers reported the value to be about 3.6 eV [93–95]. It is also noteworthy to mention, that the value of the fundamental band gap of rutile SnO₂, calculated using different calculation methods and functionals, is different: PBE, 1.75 eV; HSE06, 3.15 eV; PBE + G₀W₀, 3.33 eV; HSE06 + G₀W₀, 3.68 eV [32].

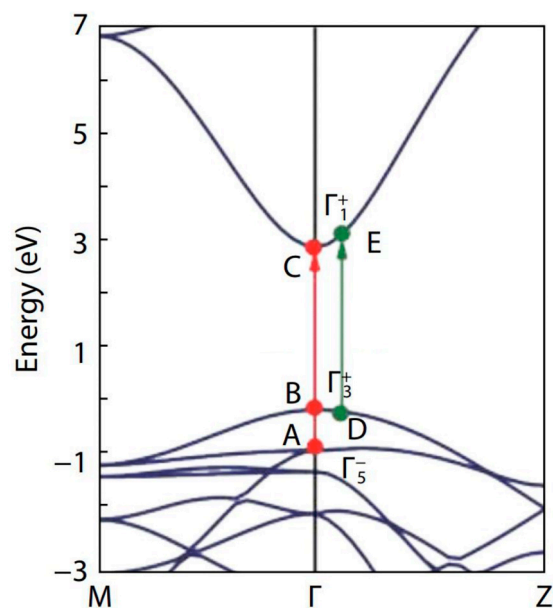


Figure 5. Band structure of SnO₂ along the two high symmetry lines M– Γ –Z. The valence band maximum is set at zero. The red and green arrows represent the possible optical transitions at Γ -point and away from Γ -point, respectively. The figure was reproduced/adapted from the work of Cai et al. (2011) [32].

To explain the fundamental and optical band gaps of SnO₂, Cai et al. [32] considered the three transition pathways: two were at the Γ -point and the other was in the vicinity of the Γ -point. They observed band gaps of 2.96 eV, 3.13 eV, and 3.69 eV for the transition paths B–C, D–E, and A–C, respectively.

In our study, the band gap of SnO₂ for the 650 °C calcination temperature, was found to be 3.00 eV, which is close to the band gap of the B–C transition [32]. Similarly, the band gap at 250 °C calcination temperature was found to be 3.11 eV, which was roughly equal to the band gap of the D–E transition. Raising the calcination temperature from 250 °C to 650 °C altered the transition path from D–E to B–C [32]. The homogeneous oxygen vacancies embedded in SnO₂ nanoparticles, induce the band gap to decrease and the valence band width to widen [96,97]. Yang et al. [96] were able to reduce the band gap from 3.81 eV to 2.53 eV, by employing oxygen vacancies. As we found an increase in the oxygen vacancies when the calcination temperature was raised from 250 °C to 650 °C, the change in the transition path in the band structure can be understood to be facilitated through the oxygen vacancies, induced by the rise in calcination temperature.

Transparent conducting oxides, such as TiO₂, ZnO, SnO₂, SiO₂, and ZrO₂, can be used as ETL [98]. To be considered as the best ETL, a film should satisfy band alignment with the perovskite layer, i.e., it should have a lower valence band and a higher conduction band than the perovskite active layer [98]. In order for a photon to easily pass through and be

absorbed by the perovskite absorber, it also requires a high transmittance in the UV-visible band [98].

Inorganic halide perovskites can be represented as ABX_3 (A = organic or inorganic monovalent cation, B = bivalent cation, X = halogen anion) [99]. The band gap of the perovskite can be changed from 0.5 eV to 4.0 eV by changes in the chemical natures of A , B , and X , as well as by variations of the crystal structure [99]. Experimentally observed band gaps of perovskite absorbers usually vary from 1.26 eV to 1.78 eV [92,100,101], which can result in a peak absorption between 300 nm and 1000 nm.

Solar absorbance in the UV–VR–IR region [44,102,103] can be written as,

$$\alpha = \frac{\int_{0.3\mu m}^{1\mu m} A(\lambda)P_{sun}(\lambda)d\lambda}{\int_{0.3\mu m}^{1\mu m} P_{sun}(\lambda)d\lambda} \quad (11)$$

where

$$P_{sun}(\lambda) = \frac{C_1}{\lambda^5 [e^{C_2/(\lambda T_{sun})} - 1]}$$

$$A(\lambda) = 1 - (T(\lambda) + R(\lambda))$$

Here, $C_1 = 3.7430 \times 10^{-16} \text{ Wm}^2$ and $C_2 = 1.4387 \times 10^{-2} \text{ mK}$. Solar spectral irradiance is best approximated by considering $T_{sun} = 5800 \text{ K}$ [44]. A , T , and R are the wavelength dependent absorbance, transmittance, and reflectance, respectively.

By the overlap of the absorbance spectrum and the solar spectrum in the wavelength range 300 nm to 1000 nm, we derived the solar absorbance. Solar absorbance was found to be 15.4%, 16.3%, and 20.1%, respectively, for thin films prepared from nanoparticles calcined at 250 °C, 450 °C, and 650 °C. Therefore, more than 79.9% solar light will pass through the thin films, which achieves the second criterion to be an ETL, as described above. As demonstrated by Meloni et al. [99], the conduction band and valence band could be tuned respectively from 0.5 eV to 1.5 eV and 0 eV to −2.5 eV, by changes in the chemical natures of A , B , and X , as well as by variations of the crystal structure. According to Cai et al. [32], the fundamental band gap of SnO_2 is 2.96 eV, with the valence band energy of 0.0 eV and conduction band energy of 2.96 eV for the B–C transition path, which was described previously. For the band gap higher than 2.96 eV, the valence band energy goes below 0.0 eV, and the conduction band energy increases above 2.96 eV, for example for the D–E transition path. As the conduction band energy of SnO_2 is much higher than that of a perovskite layer, it also satisfies the first criterion to be an ETL, as described above.

4. Conclusions

The XRD analysis confirmed the formation of highly crystalline nano-sized particles, with a tetragonal rutile structure. The FTIR spectra confirmed the presence of Sn–OH and Sn–O in the samples at low calcined temperatures. Whereas, a noticeable reduction in the Sn–OH peak was attributed to the formation of pure and dried SnO_2 powder. The EDX spectra confirmed the formation of pure SnO_2 , without any impurities. Furthermore, the SEM images showed the particles to be spherical and to form agglomerations.

The average transmittance values of the thin films were found to decrease with the increase in calcination temperatures. The band gap of the prepared SnO_2 thin films was found to decrease with increasing calcination temperature, while the oxygen vacancies and average crystallite size were found to increase with an increase in the calcination temperature. This implies that the oxygen vacancies control the morphology of the NPs and the optical and electrical properties of the thin films prepared from these NPs.

In summary, we may safely state that oxygen vacancies play a key role in tuning the structural and optical properties of SnO_2 nanoparticles and thin films.

Author Contributions: R.D. performed the experiments, analyzed, and interpreted the data of XRD, SEM, EDX, and FTIR. B.B. (Bijaya Basnet) analyzed and interpreted the data of reflectance, transmittance, XRD, FTIR, and EDX. M.P. contributed reagents, materials, and assisted in the experiments. S.B. assisted in the experiments. B.B. (Biplab Budhathoki). and S.K.T. assisted in analyzing the data of XRD, SEM, and FTIR results. K.P., B.P.K. mainly designed and supervised the project, in collaboration with S.K.T. B.B. (Bijaya Basnet) and R.D. wrote the manuscript. B.B. (Bijaya Basnet), R.D., B.P.K. and S.K.T. revised the manuscript. All authors contributed to scientific discussions. All authors have read and agreed to the published version of the manuscript.

Funding: The authors are thankful to University Grant Commission (UGC), Nepal, for grant (Collaborative Research Grant-2020) support for this research work.

Data Availability Statement: The data used to support the findings of this study will be available from the corresponding author upon request.

Acknowledgments: The authors are thankful to the Department of Natural Sciences, Kathmandu University, for providing transport and all laboratory materials and equipment facilities to carry out this research work. Tara Dhakal, Department of Electrical and Computer Engineering, Binghamton University, New York, USA for his dedicated help during research work. Central Department of Chemistry for FTIR analysis, Nepal Academy of Science and Technology (NAST) for XRD analysis, and the University of North Bengal for SEM and EDS analysis of sample characterization.

Conflicts of Interest: The authors declare no conflict of interest.

References

1. Gunkel, F.; Christensen, D.V.; Chen, Y.Z.; Pryds, N. Oxygen vacancies: The (in) visible friend of oxide electronics. *Appl. Phys. Lett.* **2020**, *116*, 120505. [[CrossRef](#)]
2. Hwang, H.Y.; Iwasa, Y.; Kawasaki, M.; Keimer, B.; Nagaosa, N.; Tokura, Y. Emergent phenomena at oxide interfaces. *Nat. Mater.* **2012**, *11*, 103–113. [[CrossRef](#)]
3. Christensen, D.V.; Trier, F.; Niu, W.; Gan, Y.; Zhang, Y.; Jespersen, T.S.; Chen, Y.; Pryds, N. Stimulating Oxide Heterostructures: A Review on Controlling SrTiO₃-Based Heterointerfaces with External Stimuli. *Adv. Mater. Interfaces* **2019**, *6*, 1900772. [[CrossRef](#)]
4. Queisser, H.J.; Haller, E.E. Defects in semiconductors: Some fatal, some vital. *Science* **1998**, *281*, 945–950. [[CrossRef](#)] [[PubMed](#)]
5. Herman, F. Electronic structure calculations of interfaces and overlayers in the 1980's. *J. Vac. Sci. Technol.* **1979**, *16*, 1101–1107. [[CrossRef](#)]
6. Lankhorst, M.H.R.; Ketelaars, B.W.S.M.M.; Wolters, R.A. Low-cost and nanoscale non-volatile memory concept for future silicon chips. *Nat. Mater.* **2005**, *4*, 347–352. [[CrossRef](#)] [[PubMed](#)]
7. Merkle, R.; Maier, J. How is oxygen incorporated into oxides? A comprehensive kinetic study of a simple solid-state reaction with SrTiO₃ as a model material. *Angew. Chem. Int. Ed.* **2008**, *47*, 3874–3894. [[CrossRef](#)] [[PubMed](#)]
8. Ganduglia-Pirovano, M.V.; Hofmann, A.; Sauer, J. Oxygen vacancies in transition metal and rare earth oxides: Current state of understanding and remaining challenges. *Surf. Sci. Rep.* **2007**, *62*, 219–270. [[CrossRef](#)]
9. De Souza, R.A. Oxygen diffusion in SrTiO₃ and related perovskite oxides. *Adv. Funct. Mater.* **2015**, *25*, 6326–6342. [[CrossRef](#)]
10. Frederikse, H.P.R.; Hosler, W.R. Hall Mobility in SrTiO₃. *Phys. Rev.* **1967**, *161*, 822. [[CrossRef](#)]
11. Das, S.; Jayaraman, V. SnO₂: A comprehensive review on structures and gas sensors. *Prog. Mater. Sci.* **2014**, *66*, 112–255. [[CrossRef](#)]
12. Choudhury, Biswajit, and Amarjyoti Choudhury. Ce³⁺ and oxygen vacancy mediated tuning of structural and optical properties of CeO₂ nanoparticles. *Mater. Chem. Phys.* **2012**, *131*, 666–671. [[CrossRef](#)]
13. Zeng, Q.; Cui, Y.; Zhu, L.; Yao, Y. Increasing oxygen vacancies at room temperature in SnO₂ for enhancing ethanol gas sensing. *Mater. Sci. Semicond. Process.* **2020**, *111*, 104962. [[CrossRef](#)]
14. Wei, Y.; Chen, C.; Yuan, G.; Gao, S. SnO₂ nanocrystals with abundant oxygen vacancies: Preparation and room temperature NO₂ sensing. *J. Alloys Compd.* **2016**, *681*, 43–49. [[CrossRef](#)]
15. Sahu, B.K.; Das, A. Significance of in-plane oxygen vacancy rich non-stoichiometric layer towards unusual high dielectric constant in nano-structured SnO₂. *Phys. E Low-Dimens. Syst. Nanostructures* **2018**, *103*, 60–65. [[CrossRef](#)]
16. Schipani, F.; Ponce, M.A.; Joanni, E.; Williams, F.J.; Aldao, C.M. Study of the oxygen vacancies changes in SnO₂ polycrystalline thick films using impedance and photoemission spectroscopies. *J. Appl. Phys.* **2014**, *116*, 194502. [[CrossRef](#)]
17. Choi, E.; Lee, D.; Shin, H.-J.; Kim, N.; De Los Santos Valladares, L.; Seo, J. Role of oxygen vacancy sites on the temperature-dependent photoluminescence of SnO₂ nanowires. *J. Phys. Chem. C* **2021**, *125*, 14974–14978. [[CrossRef](#)]
18. Kumaravel, V.; Bianchetti, E.; Mathew, S.; Hinder, S.J.; Bartlett, J.; Di Valentin, C.; Pillai, S.C. New Insights into Crystal Defects, Oxygen Vacancies, and Phase Transition of Ir-TiO₂. *J. Phys. Chem. C* **2021**, *125*, 23548–23560. [[CrossRef](#)]
19. Ischenko, V.; Polarz, S.; Grote, D.; Stavarache, V.; Fink, K.; Driess, M. Zinc oxide nanoparticles with defects. *Adv. Funct. Mater.* **2005**, *15*, 1945–1954. [[CrossRef](#)]
20. Mahmood, Q.; Afzal, A.; Siddiqi, H.M.; Habib, A. Sol-gel synthesis of tetragonal ZrO₂ nanoparticles stabilized by crystallite size and oxygen vacancies. *J. Sol-Gel Sci. Technol.* **2013**, *67*, 670–674. [[CrossRef](#)]

21. Zhang, X.; Tang, F.; Wang, M.; Zhan, W.; Hu, H.; Li, Y.; Friend, R.H.; Song, X. Femtosecond visualization of oxygen vacancies in metal oxides. *Sci. Adv.* **2020**, *6*, eaax9427. [[CrossRef](#)]
22. Zhu, S.; Shi, S.; Zheng, X.; Wang, X.; Yu, G.; Jiang, Y.; Feng, J.; Zhu, L.; Zhang, G. Enhanced Oxygen Vacancies in Ce-Doped SnO₂ Nanofibers for Highly Efficient Soot Catalytic Combustion. *Catalysts* **2022**, *12*, 596. [[CrossRef](#)]
23. Elouafi, A.; Moubah, R.; Tizliouine, A.; Derkaoui, S.; Omari, L.H.; Lassri, H. Effects of Ru doping and of oxygen vacancies on the optical properties in α -Fe₂O₃ powders. *Appl. Phys. A* **2020**, *126*, 228. [[CrossRef](#)]
24. Liu, J.; Gao, F.; Wu, L.; Zhang, H.; Hong, W.; Jin, G.; Zhai, Z.; Fu, C. Size effect on oxygen vacancy formation and gaseous adsorption in ZnO nanocrystallites for gas sensors: A first principle calculation study. *Appl. Phys. A* **2020**, *126*, 454. [[CrossRef](#)]
25. Ahn, M.-W.; Park, K.-S.; Heo, J.-H.; Park, J.-G.; Kim, D.-W.; Choi, K.J.; Lee, J.-H.; Hong, S.-H. Gas sensing properties of defect-controlled ZnO-nanowire gas sensor. *Appl. Phys. Lett.* **2008**, *93*, 263103. [[CrossRef](#)]
26. Teng, F.; Li, M.; Gao, C.; Zhang, G.; Zhang, P.; Wang, Y.; Chen, L.; Xie, E. Preparation of black TiO₂ by hydrogen plasma assisted chemical vapor deposition and its photocatalytic activity. *Appl. Catal. B Environ.* **2014**, *148*, 339–343. [[CrossRef](#)]
27. Han, D.; Jiang, B.; Feng, J.; Yin, Y.; Wang, W. Photocatalytic Self-Doped SnO_{2-x} Nanocrystals Drive Visible-Light-Responsive Color Switching. *Angew. Chem. Int. Ed.* **2017**, *56*, 7792–7796. [[CrossRef](#)]
28. Wang, C.; Wu, D.; Wang, P.; Ao, Y.; Hou, J.; Qian, J. Effect of oxygen vacancy on enhanced photocatalytic activity of reduced ZnO nanorod arrays. *Appl. Surf. Sci.* **2015**, *325*, 112–116. [[CrossRef](#)]
29. Ou, G.; Xu, Y.; Wen, B.; Lin, R.; Ge, B.; Tang, Y.; Liang, Y.; Yang, C.; Huang, K.; Zu, D.; et al. Tuning defects in oxides at room temperature by lithium reduction. *Nat. Commun.* **2018**, *9*, 1302. [[CrossRef](#)]
30. Liu, S.; Gao, S.; Wang, Z.; Fei, T.; Zhang, T. Oxygen vacancy modulation of commercial SnO₂ by an organometallic chemistry-assisted strategy for boosting acetone sensing performances. *Sens. Actuators B Chem.* **2019**, *290*, 493–502. [[CrossRef](#)]
31. Li, Y.; Zu, B.; Guo, Y.; Li, K.; Zeng, H.; Dou, X. Surface Superoxide Complex Defects-Boosted Ultrasensitive ppb-Level NO₂ Gas Sensors. *Small* **2016**, *12*, 1420–1424. [[CrossRef](#)] [[PubMed](#)]
32. Cai, X.; Zhang, P.; Wei, S.-H. Revisit of the band gaps of rutile SnO₂ and TiO₂: A first-principles study. *J. Semicond.* **2019**, *40*, 092101. [[CrossRef](#)]
33. Batzill, M.; Diebold, U. The surface and materials science of tin oxide. *Prog. Surf. Sci.* **2005**, *79*, 47–154. [[CrossRef](#)]
34. Ganose, A.M.; Scanlon, D.O. Band gap and work function tailoring of SnO₂ for improved transparent conducting ability in photovoltaics. *J. Mater. Chem. C* **2016**, *4*, 1467–1475. [[CrossRef](#)]
35. Sarangi, S.; Pradhan, G.K.; Samal, D. Band gap engineering in SnO₂ by Pb doping. *J. Alloys Compd.* **2018**, *762*, 16–20. [[CrossRef](#)]
36. Sarmah, S.; Kumar, A. Optical properties of SnO₂ nanoparticles. *Indian J. Phys.* **2010**, *84*, 1211–1221. [[CrossRef](#)]
37. Kamble, V.B.; Umarji, A.M. Defect induced optical bandgap narrowing in undoped SnO₂ nanocrystals. *AIP Adv.* **2013**, *3*, 082120. [[CrossRef](#)]
38. Popov, A.; Kotomin, E.; Maier, J. Basic properties of the F-type centers in halides, oxides and perovskites. *Nucl. Instrum. Methods Phys. Res. Sect. B Beam Interact. Mater. At.* **2010**, *268*, 3084–3089. [[CrossRef](#)]
39. Naje, A.N.; Norry, A.S.; Suhail, A.M. Preparation and characterization of SnO₂ nanoparticles. *Int. J. Innov. Res. Sci. Eng. Technol.* **2013**, *2*, 7068–7072.
40. Kafle, M.; Kapadi, R.K.; Joshi, L.P.; Rajbhandari, A.; Subedi, D.P.; Gyawali, G.; Lee, S.W.; Adhikari, R.; Kafle, B.P. Effect of calcination environments and plasma treatment on structural, optical and electrical properties of FTO transparent thin films. *AIP Adv.* **2017**, *7*, 075101. [[CrossRef](#)]
41. Patil, E.G.; Kajale, D.D.; Gaikwad, V.B.; Jain, G.H. Preparation and characterization of SnO₂ nanoparticles by hydrothermal route. *Int. Nano Lett.* **2012**, *2*, 17. [[CrossRef](#)]
42. Senthilkumar, V.; Vickraman, P.; Jayachandran, M.; Sanjeeviraja, C. Synthesis and characterization of SnO₂ nanopowder prepared by precipitation method. *J. Dispers. Sci. Technol.* **2010**, *31*, 1178–1181. [[CrossRef](#)]
43. Cullity, B.D. *Elements of X-ray Diffraction*; Addison-Wesley Publishing: Boston, MA, USA, 1956.
44. Kafle, B.P.; Basnet, B.; Timalsina, B.; Deo, A.; Malla, T.N.; Acharya, N.; Adhikari, A. Optical, structural and thermal performances of black nickel selective coatings for solar thermal collectors. *Sol. Energy* **2022**, *234*, 262–274. [[CrossRef](#)]
45. Rac, O.; Suchorska-Woźniak, P.; Fiedot, M.; Teterycz, H. Influence of stabilising agents and pH on the size of SnO₂ nanoparticles. *Beilstein J. Nanotechnol.* **2014**, *5*, 2192–2201. [[CrossRef](#)]
46. Hossain, M.Z.; Halder, S.; Ahmed, A.N.; Gafur, A. Synthesis of spherical silver nanoparticles by chemical reduction method. *J. Bangladesh Chem. Soc.* **2018**, *30*, 2.
47. Langford, J.I.; Wilson, A.J.C. Wilson. Scherrer after sixty years: A survey and some new results in the determination of crystallite size. *J. Appl. Crystallogr.* **1978**, *11*, 102–113. [[CrossRef](#)]
48. Lele, S.; Anantharaman, T.R. Influence of crystallite shape on particle size broadening of Debye-Scherrer reflections. In *Proceedings of the Indian Academy of Sciences-Section A*; Springer: New Delhi, India, 1966; Volume 64.
49. Patterson, A.L. The Scherrer formula for X-ray particle size determination. *Phys. Rev.* **1939**, *56*, 978. [[CrossRef](#)]
50. Short, M.; Walker, P., Jr. Measurement of interlayer spacings and crystal sizes in turbostratic carbons. *Carbon* **1963**, *1*, 3–9. [[CrossRef](#)]
51. Muniz, F.T.L.; Miranda, M.A.R.; dos Santos, C.M.; Sasaki, J.M. The Scherrer equation and the dynamical theory of X-ray diffraction. *Acta Crystallogr. Sect. A Found. Adv.* **2016**, *72*, 385–390. [[CrossRef](#)]

52. Londoño-Restrepo, S.M.; Jeronimo-Cruz, R.; Millán-Malo, B.M.; Rivera-Muñoz, E.M.; Rodríguez-García, M.E. Effect of the nano crystal size on the X-ray diffraction patterns of biogenic hydroxyapatite from human, bovine, and porcine bones. *Sci. Rep.* **2019**, *9*, 5915. [[CrossRef](#)] [[PubMed](#)]
53. Mongkolsuttirat, K.; Buajarern, J. Uncertainty evaluation of crystallite size measurements of nanoparticle using X-Ray Diffraction analysis (XRD). *J. Phys. Conf. Series.* **2021**, *1719*, 012054. [[CrossRef](#)]
54. Lima, F.M.; Martins, F.M.; Maia, P.H.F., Jr.; Almeida, A.F.L.; Freire, F.N.A. Nanostructured titanium dioxide average size from alternative analysis of Scherrer's Equation. *Matéria* **2018**, *23*, 1–9. [[CrossRef](#)]
55. Smilgies, D.-M. Scherrer grain-size analysis adapted to grazing-incidence scattering with area detectors. *J. Appl. Crystallogr.* **2009**, *42*, 1030–1034. [[CrossRef](#)]
56. Bakr, N.A.; Salman, S.A.; Ali, M.N. Role of substrate temperature on the structural and optical properties of chemically sprayed SnO₂ thin films. *Dig. J. Nanomater. Biostructures (DJNB)* **2019**, *14*, 517–525.
57. Khaenamkaew, P.; Manop, D.; Tanghengjaroen, C.; Ayuthaya, W.P.N. Crystal structure, lattice strain, morphology, and electrical properties of SnO₂ nanoparticles induced by low calcination temperature. *Adv. Mater. Sci. Eng.* **2020**, *2020*, 3852421. [[CrossRef](#)]
58. Choudhury, S.P.; Kumari, N.; Bhattacharjee, A. Comparative X-ray diffraction study of SnO₂ nanoparticle samples from different precursor solutions. *Cell* **2014**, *69*, 71–281.
59. Fatimah, S.; Ragadhita, R.; Al Husaeni, D.F.; Nandiyanto, A.B.D. How to calculate crystallite size from X-ray diffraction (XRD) using Scherrer method. *ASEAN J. Sci. Eng.* **2010**, *2*, 65–76. [[CrossRef](#)]
60. Vinila, V.; Isac, J. Synthesis and structural studies of superconducting perovskite GdBa₂Ca₃Cu₄O_{10.5+δ} nanosystems. In *Design, Fabrication, and Characterization of Multifunctional Nanomaterials*; Elsevier: Amsterdam, The Netherlands, 2022; pp. 319–341.
61. Savio, A.K.; Starikov, D.; Bensaoula, A.; Pillai, R.; García, L.L.D.L.T.; Hernández, F.C.R. Tunable TiO₂ (anatase and rutile) materials manufactured by mechanical means. *Ceram. Int.* **2012**, *38*, 3529–3535. [[CrossRef](#)]
62. Gatea, A.H. Impact of sintering temperature on crystallite size and optical properties of SnO₂ nanoparticles. *J. Phys. Conf. Series.* **2021**, *1829*, 012030. [[CrossRef](#)]
63. Habte, A.G.; Hone, F.G.; Dejene, F.B. Effect of solution pH on structural, optical and morphological properties of SnO₂ nanoparticles. *Phys. B Condens. Matter* **2020**, *580*, 411832. [[CrossRef](#)]
64. Kumar, V.; Singh, K.; Singh, K.; Kumari, S.; Kumar, A.; Thakur, A. Effect of solvent on the synthesis of SnO₂ nanoparticles. *AIP Conf. Proc.* **2016**, *1728*, 020532.
65. López Morales, F.; Zayas, T.; Contreras, O.E. Effect of Sn precursor on the synthesis of SnO₂ and Sb-doped SnO₂ particles via polymeric precursor method. *Front. Mater. Sci.* **2013**, *7*, 387–395. [[CrossRef](#)]
66. Loksha, H.S.; Mohanty, P.; Prinsloo, A.R.E.; Sheppard, C.J. Sheppard Impact of Cr doping on the structure, optical and magnetic properties of nanocrystalline ZnO particles. *arXiv* **2021**, arXiv:2111.07264.
67. Zhu, J.-J.; Zhu, J.-M.; Liao, X.-H.; Fang, J.-L.; Zhou, M.-G.; Chen, H.-Y. Rapid synthesis of nanocrystalline SnO₂ powders by microwave heating method. *Mater. Lett.* **2002**, *53*, 12–19. [[CrossRef](#)]
68. Al-Hada, N.M.; Kamari, H.M.; Baqer, A.A.; Shaari, A.H.; Saion, E. Thermal calcination-based production of SnO₂ nanopowder: An analysis of SnO₂ nanoparticle characteristics and antibacterial activities. *Nanomaterials* **2018**, *8*, 250. [[CrossRef](#)] [[PubMed](#)]
69. Ahmad, T.B.; Asif, A.B.; Khurshid, W.A.; Masood, A.K.; Ahmad, S.G. Preparation-Characterization-SnO₂-Nanoparticles-Antibacterial-Properties-nmct-20-104. *Nanomater. Chem. Technol.* **2020**, 1–5. [[CrossRef](#)]
70. Zulfiqar, Khan, R.; Yuan, Y.; Iqbal, Z.; Yang, J.; Wang, W.; Ye, Z.; Lu, J. Variation of structural, optical, dielectric and magnetic properties of SnO₂ nanoparticles. *J. Mater. Sci. Mater. Electron.* **2017**, *28*, 4625–4636. [[CrossRef](#)]
71. Choudhury, B.; Chetri, P.; Choudhury, A. Annealing temperature and oxygen-vacancy-dependent variation of lattice strain, band gap and luminescence properties of CeO₂ nanoparticles. *J. Exp. Nanosci.* **2015**, *10*, 103–114. [[CrossRef](#)]
72. Qin, W.; Nagase, T.; Umakoshi, Y.; Szpunar, J. Relationship between microstrain and lattice parameter change in nanocrystalline materials. *Philos. Mag. Lett.* **2008**, *88*, 169–179. [[CrossRef](#)]
73. Baeumer, C.; Funck, C.; Locatelli, A.; Mentş, T.O.; Genuzio, F.; Heisig, T.; Hensling, F.; Raab, N.; Schneider, C.M.; Menzel, S.; et al. In-gap states and band-like transport in memristive devices. *Nano Lett.* **2018**, *19*, 54–60. [[CrossRef](#)]
74. Schütz, P.; Christensen, D.V.; Borisov, V.; Pfaff, F.; Scheiderer, P.; Dudy, L.; Zapf, M.; Gabel, J.; Chen, Y.Z.; Pryds, N.; et al. Microscopic origin of the mobility enhancement at a spinel/perovskite oxide heterointerface revealed by photoemission spectroscopy. *Phys. Rev. B* **2017**, *96*, 161409. [[CrossRef](#)]
75. Gunkel, F.; Jin, L.; Mueller, D.N.; Hausner, C.; Bick, D.S.; Jia, C.-L.; Schneller, T.; Valov, I.; Waser, R.; Dittmann, R. Ordering and phase control in epitaxial double-perovskite catalysts for the oxygen evolution reaction. *ACS Catal.* **2017**, *7*, 7029–7037. [[CrossRef](#)]
76. Tufte, O.N.; Chapman, P.W. Electron mobility in semiconducting strontium titanate. *Phys. Rev.* **1967**, *155*, 796. [[CrossRef](#)]
77. Moos, R.; Härdtl, K.H. Electronic transport properties of Sr_{1-x}La_xTiO₃ ceramics. *J. Appl. Phys.* **1996**, *80*, 393–400. [[CrossRef](#)]
78. Minkov, D.A. Calculation of the optical constants of a thin layer upon a transparent substrate from the reflection spectrum. *J. Phys. D Appl. Phys.* **1989**, *22*, 1157. [[CrossRef](#)]
79. Swanepoel, R. Determination of the thickness and optical constants of amorphous silicon. *J. Phys. E Sci. Instrum.* **1983**, *16*, 1214. [[CrossRef](#)]
80. Keradec, J. Thesis L'Universite Scientifique et Medicale de Grenoble. 1973.
81. Mini, A. Thesis L'Universite Scientifique et Medicale de Grenoble. 1982.
82. Heavens, O.S.; Singer, S.F. *Optical Properties of Thin Solid Films*; Courier Corporation: North Chelmsford, MA, USA, 1991.

83. Korampally, V.; Yun, M.; Rajagopalan, T.; Dasgupta, P.K.; Gangopadhyay, K.; Gangopadhyay, S. Entropy driven spontaneous formation of highly porous films from polymer–nanoparticle composites. *Nanotechnology* **2009**, *20*, 425602. [[CrossRef](#)]
84. Kushev, D.; Zheleva, N.; Demakopoulou, Y.; Siapkias, D. A new method for the determination of the thickness, the optical constants and the relaxation time of weakly absorbing semiconducting thin films. *Infrared Phys.* **1986**, *26*, 385–393. [[CrossRef](#)]
85. Borah, D.J.; Mostako, A.; Saikia, P.; Dutta, P. Effect of thickness and post deposition annealing temperature on the structural and optical properties of thermally evaporated molybdenum oxide films. *Mater. Sci. Semicond. Process.* **2019**, *93*, 111–122. [[CrossRef](#)]
86. Green, T.M.; Hadley, L.N. Tolansky Gauge for Rapid Measurement of Film Thickness. *JOSA* **1955**, *45*, 228–229. [[CrossRef](#)]
87. Gnanam, S.; Rajendran, V. Luminescence properties of EG-assisted SnO₂ nanoparticles by sol-gel process. *Dig. J. Nanomater. Biostructures* **2010**, *5*, 699–704.
88. Xin, Z.; Xiao-Hui, S.; Dian-Lin, Z. Thickness dependence of grain size and surface roughness for dc magnetron sputtered Au films. *Chin. Phys. B* **2010**, *19*, 086802. [[CrossRef](#)]
89. El-Nahass, M.M.; El-Menyawy, E.M. Thickness dependence of structural and optical properties of indium tin oxide nanofiber thin films prepared by electron beam evaporation onto quartz substrates. *Mater. Sci. Eng. B* **2012**, *177*, 145–150. [[CrossRef](#)]
90. Tauc, J. *Optical properties of amorphous semiconductors. Amorphous and Liquid Semiconductors*; Springer: Boston, MA, USA, 1974; pp. 159–220.
91. Pandey, M.; Hamal, D.; Subedi, D.; Basnet, B.; Sah, R.; Tiwari, S.K.; Kafle, B. Deposition of Reduced Graphene Oxide Thin Film by Spray Pyrolysis Method for Perovskite Solar Cell. *arXiv* **2022**, arXiv:2212.01066. [[CrossRef](#)]
92. Pandey, M.; Hamal, D.; Basnet, B.; Kafle, B. Synthesis and optical characterization of perovskite layer for solar cell application. *arXiv* **2022**, arXiv:2211.13410. [[CrossRef](#)]
93. Schleife, A.; Varley, J.B.; Fuchs, F.; Rödl, C.; Bechstedt, F.; Rinke, P.; Janotti, A.; Van de Walle, C.G. Tin dioxide from first principles: Quasiparticle electronic states and optical properties. *Phys. Rev. B* **2011**, *83*, 035116. [[CrossRef](#)]
94. Jiang, Q.; Zhang, L.; Wang, H.; Yang, X.; Meng, J.; Liu, H.; Yin, Z.; Wu, J.; Zhang, X.; You, J. Enhanced electron extraction using SnO₂ for high-efficiency planar-structure HC (NH₂)₂PbI₃-based perovskite solar cells. *Nat. Energy* **2016**, *2*, 16177. [[CrossRef](#)]
95. Scanlon, D.O.; Dunnill, C.W.; Buckeridge, J.; Shevlin, S.A.; Logsdail, A.J.; Woodley, S.M.; Catlow, C.R.A.; Powell, M.J.; Palgrave, R.G.; Parkin, I.P.; et al. Band alignment of rutile and anatase TiO₂. *Nat. Mater.* **2013**, *12*, 798–801. [[CrossRef](#)]
96. Yang, Y.; Wang, Y.; Yin, S. Oxygen vacancies confined in SnO₂ nanoparticles for desirable electronic structure and enhanced visible light photocatalytic activity. *Appl. Surf. Sci.* **2017**, *420*, 399–406. [[CrossRef](#)]
97. Noh, M.F.M.; Arzaee, N.A.; Safaei, J.; Mohamed, N.A.; Kim, H.P.; Yusoff, A.R.M.; Jang, J.; Teridi, M.A.M. Eliminating oxygen vacancies in SnO₂ films via aerosol-assisted chemical vapour deposition for perovskite solar cells and photoelectrochemical cells. *J. Alloys Compd.* **2019**, *773*, 997–1008.
98. Mahmood, K.; Sarwar, S.; Mehran, M.T. Current status of electron transport layers in perovskite solar cells: Materials and properties. *RSC Adv.* **2017**, *7*, 17044–17062. [[CrossRef](#)]
99. Meloni, S.; Palermo, G.; Ashari-Astani, N.; Grätzel, M.; Rothlisberger, U. Valence and conduction band tuning in halide perovskites for solar cell applications. *J. Mater. Chem. A* **2016**, *4*, 15997–16002. [[CrossRef](#)]
100. Prasanna, R.; Gold-Parker, A.; Leijtens, T.; Conings, B.; Babayigit, A.; Boyen, H.-G.; Toney, M.F.; McGehee, M.D. Band gap tuning via lattice contraction and octahedral tilting in perovskite materials for photovoltaics. *J. Am. Chem. Soc.* **2017**, *139*, 11117–11124. [[CrossRef](#)]
101. Abdollahi Nejad, B.; Ritzer, D.B.; Hu, H. Scalable two-terminal all-perovskite tandem solar modules with a 19.1% efficiency. *Nat. Energy* **2022**, *7*, 620–630. [[CrossRef](#)]
102. Lizama-Tzec, F.; Herrera-Zamora, D.; Arés-Muzio, O.; Gómez-Espinoza, V.; Santos-González, I.; Cetina-Dorantes, M.; Vega-Poot, A.; García-Valladares, O.; Oskam, G. Electrodeposition of selective coatings based on black nickel for flat-plate solar water heaters. *Sol. Energy* **2019**, *194*, 302–310. [[CrossRef](#)]
103. Lizama-Tzec, F.I.; Macias, J.D.; Estrella-Gutiérrez, M.A.; Cahue-López, A.C.; Arés, O.; de Coss, R.; Alvarado-Gil, J.J.; Oskam, G. Electrodeposition and characterization of nanostructured black nickel selective absorber coatings for solar–thermal energy conversion. *J. Mater. Sci. Mater. Electron.* **2015**, *26*, 5553–5561. [[CrossRef](#)]

Disclaimer/Publisher’s Note: The statements, opinions and data contained in all publications are solely those of the individual author(s) and contributor(s) and not of MDPI and/or the editor(s). MDPI and/or the editor(s) disclaim responsibility for any injury to people or property resulting from any ideas, methods, instructions or products referred to in the content.